Journal of Controlled Release 383 (2025) 113779

Contents lists available at ScienceDirect

Journal of Controlled Release

journal homepage: www.elsevier.com/locate/jconrel

Sequentially conquering transfection obstacles of primary human T cells via non-classical lipid nanoparticles delivering reformative transposon system

Mengtong Wu [1], Jingwen Li [1], Yazhou Xu, Shaoxiong Lv, Guan Wang, Yingshuang Huang, Yu Tao, Caoyun Ju [*], Can Zhang [*]

State Key Laboratory of Natural Medicines, Jiangsu Key Laboratory of Drug Discovery for Metabolic Diseases, Center of Advanced Pharmaceuticals and Biomaterials, China Pharmaceutical University, Nanjing 211198, PR China

ARTICLE INFO

Keywords:
Lipids
Lipid nanoparticles
CAR-T construction
Plasmid transfection
PiggyBac transposon
Molecular dynamics

ABSTRACT

Chimeric antigen receptor (CAR)-T cells have shown promising efficacy in disease treatment. Considering the safety issues of viral vectors, non-viral vectors such as lipid nanoparticles (LNPs) or transposon systems have attracted growing attention in constructing CAR-T cells. However, the limited transfection efficiency of LNPs and the possible cellular damage via electroporation of transposon system restrict their applications. Herein, we propose to construct CAR-T cells with long-lasting CAR expression via non-classical LNPs delivering reformative piggyBac transposon system. The non-classical LNPs (TA7AD8 LNPs) significantly enhance the cellular uptake by T cells and promote lysosomal escape due to the engagement of novel lipid (AD8) holding asymmetric tails. To further improve the transfection efficiency of transposon, we modify the transposon through inserting a nuclear-targeting sequence and reducing the molecular size to gain a minicircle nuclear location piggyBac transposon system. Based on these, we successfully construct the CD19 CAR-T with long-lasting CAR expression and potent cytotoxicity, achieving antitumor efficacy comparable to that by lentivirus. This work provides a safe, facile, and effective approach for in vitro engineering CAR-T cells, which can be applied in the future to avoid the safety concerns of viral vectors, lower the price, and shorten the manufacturing period of CAR-T cells.

1. Introduction

Chimeric antigen receptor (CAR) T-cell therapy, as a new-paradigm immunotherapy, has given rise to breakthroughs in treatment of malignant tumors [1], autoimmune diseases [2], myocardial damage [3], and so on [4]. All the clinical CAR-T products are ex vivo constructed by viral vectors [5] to gain persistent CAR expression. However, FDA recently reported the possible serious risk of T cell malignancy following BCMA-directed or CD19-directed autologous CAR-T cell therapy owing to the viral vectors that can be inserted into the host cell genomes. More than that, viral vectors face the limitations of limited capacity, high cost, and immunogenicity. [6] Therefore, non-viral vectors for engineering persistent CAR-T cells show promise.

Transposon system, an emerging non-viral system, such as Sleeping Beauty (SB) and piggyBac (PB), can achieve stable gene expression by a cut-and-paste mechanism [7], which is usually introduced into cells via electroporation. It has been harnessed for constructing CAR-T cells with long-lasting CAR expression in clinical trials [8]. However, the uncertain loss of cytoplasmic inclusions during the electroporation process and the resulting low cell viability after electroporation might affect the efficacy of CAR-T cells [9]. By comparison, lipid nanoparticle (LNP) is a non-viral vector for gene delivery, which has received growing attention due to low toxicity, superior biocompatibility, and cost-effectiveness [10], especially after the approval of the first siRNA drug Onpattro™ and two COVID-19 vaccines [11]. Thus, delivering a transposon system into primary T cells via LNPs might be an available approach for constructing long-lasting CAR-T cells. However, the extremely low transfection efficacy of LNPs delivering transposon system for CAR transfection, which is only 4.5 % to our best knowledge [12], hampers their future application.

To address the challenges, the obstacles of engineering long-persisting CAR-T cells via traditional LNPs can be ascribed to three reasons. Firstly, as a kind of non-phagocytic lymphocyte, T cells cannot actively phagocytose large amounts of exogenous materials [13,14],

* Corresponding authors.
E-mail addresses: jucaoyun@cpu.edu.cn (C. Ju), zhangcan@cpu.edu.cn (C. Zhang).
[1] Authors contributed equally to this work.

https://doi.org/10.1016/j.jconrel.2025.113779
Received 4 December 2024; Received in revised form 23 April 2025; Accepted 24 April 2025
Available online 28 April 2025

which limits the entry of LNP into T cells. Secondly, transposons within LNP must escape from the endo/lysosomes to avoid degradation [15], while the escape ratio of LNP is below 15 % [16]. The last one is that the transposon system should enter the cell nucleus to take effect, whereas the viscous cytosol hampers the free movement of transposon towards the nucleus, and the small nuclear pore restricts the entry of large transposon system (usually larger than 7000 bp).

Herein, we were supposed to sequentially conquer these obstacles via developing a non-classical LNP and an optimized transposon for effective construction of long-lasting CAR-T cells (Fig. 1). We first designed a series of asymmetric tails-based functional lipids (adamantane lipid, AD), as the fifth functional lipid whose adamantane tail has demonstrated the tropism to T cells [17]. Afterward, a top-performing LNP (TA7AD8 LNP) composed of ionizable lipid of TA7 (an ionizable lipid with glutamic acid as a linkage designed by our group), adamantane lipid (AD8, as the fifth functional lipid), neutral phospholipid of 1,2-dioleoyl-sn-glycero-3-phosphoethanolamine (DOPE), cholesterol, and PEGylated lipid of PEG_{2000}-Succinic anhydride-ditetradecyl glutamate (PEG_{2000}-Suc-TA_2, a novel PEGylated lipid designed by our group) was screened, which exhibited the superior transfection efficiency of green fluorescent protein (GFP) pDNA into $CD3^+$ primary T cells up to 18.3 %, about 2.3-fold than that has been reported [18]. Further, we found that the endocytosis of TA7AD8 LNP by T cells was significantly increased due to the reduced particle size after AD8 engagement in LNP. Moreover, AD8 could increase the membrane fusion through enhancing the membrane fluidity and inducing more lipid packing defects to reduce the energy barrier during membrane fusion. Besides, we found that the low pK_a of TA7AD8 LNP

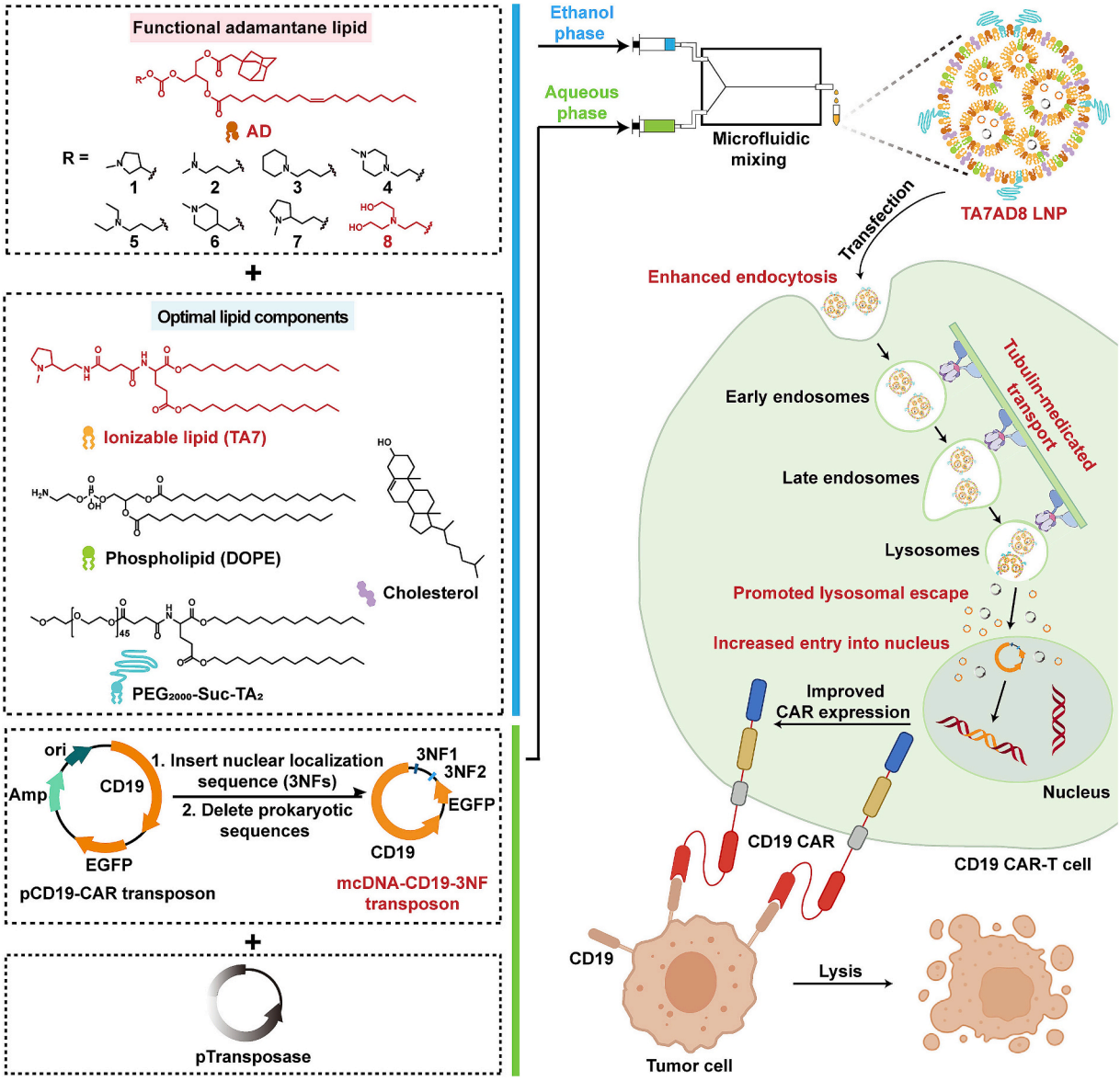

Fig. 1. Schematic illustration of the preparation and mechanism of non-classical LNP delivering transposon system for ex vivo engineering CAR-T cells. The functional adamantane lipids (AD1-AD8), ionizable lipid (TA7), and PEGylated lipid (PEG_{2000}-Suc-TA_2) were newly synthesized. Of which, the complex of AD8 and TA7, along with DOPE, cholesterol, and PEG_{2000}-Suc-TA_2 were optimized for the preparation of the top-performing TA7AD8 LNP via the microfluidic method, which showed a high transfection efficiency of pDNA in primary T cells by enhancing endocytosis, promoting lysosomal escape, and increasing the concentration of pDNA around nucleus via tubulin-mediated intracellular transport. To further improve the pDNA into the nucleus, the conventional PB transposon (pCD19-CAR, 7824 bp) was remodeled by inserting nuclear localization sequence (3NFs) and deleting prokaryotic sequences, thereby generating the minicircle nuclear location transposon (mcDNA-CD19 3NF, 5235 bp). Based on these, TA7AD8 LNP successfully transfected primary T cells by co-delivering mcDNA-CD19-3NF and a transposase plasmid, thus achieving CD19 CAR-T cells with a high CAR positive ratio and long-lasting CAR expression, which showed potent cytotoxicity against $CD19^+$ Tumor cells.

favored the pDNA escape from lysosomes near the nucleus, which leveraged the tubulin movement to deliver pDNA around the nucleus, thus circumventing the long-distance movement in viscous cytosol. Finally, to promote the entry of large transposons into the nucleus, a minicircle nuclear location transposon (mcDNA-CD19-3NF) was designed and constructed through modifying the conventional PB transposon into a shortened sequence with a nuclear targeting sequence. Thus, TA7AD8 LNP delivering mcDNA-CD19-3NF and a transposase plasmid into primary human $CD3^+$T cells achieved a positive ratio of 10.8 % of CD19 CAR and with a persisted CAR expression at least 15 days, while that transfected by Lipofectamine 2000 was only 0.89 %. The physiological functions of CD19 CAR-T cells, such as proliferation, viability, and phenotype maintained after transfection via TA7AD8 LNP, as well as the potent cytotoxicity against $CD19^+$ tumor cells. In short, TA7AD8 LNP delivering the minicircle nuclear location transposon has the application prospect to engineer CAR-T cells in a safe, simple, facile, and cost-effective manner in the future.

2. Materials and methods

2.1. Materials

All chemical agents for lipid synthesis were purchased from Bide Pharmtech Ltd. Cholesterol, 1,2-dioleoyl-sn-glycero-3-phosphoethanolamine (DOPE), 1, 2-dioleoyl-*sn*-glycero-3-phosphocholine (DOPC), soy phosphatidylcholine (SPC), 1,2-dioctadecanoyl-*sn*-glycero-3-phophocholine (DSPC), 1, 2-dimyristoyl-*sn*-glycero-3-phosphocholine (DMPC), 1, 2-distearoyl-*sn*-glycero-3-phosphoethanolamine (DSPE), and 1, 2-dipalmitoyl-*sn*-glycero-3-phosphoethanolamine (DPPE) were purchased from AVT (shanghai) Pharmaceutical Tech Co. All of them were used as received. PmaxGFP was purchased from Lonza. Ultra GelRed, Annexin V-PE/7-AAD Apoptosis Detection Kit, and Phanta Max Super-Fidelity DNA Polymerase were purchased from Vazyme. Human peripheral blood lymphocyte separation medium was purchased from TBD science. ImmunoCult™-XF T cell medium, ImmunoCult™ human CD3/CD28 T cell activator, recombinant human IL-2, and EasySep™ human T cell isolation kit were purchased from STEMCELL. Fetal bovine serum (FBS) and Roswell Park Memorial Institute (RPMI) 1640 medium were purchased from Gibco. Dulbecco's modified eagle medium (DMEM) was purchased from HyClone. All of the antibodies were purchased from BioLegend. All of the endonuclease were purchased from Adamas life. Phosphotungstic acid was purchased from Yonghua Chemical Co. CFDA SE staining kit, LDH cytotoxicity assay kit, ionomycin, phorbol-12-myristate-13-acetate, brefeldin, Lyso-tracker green, and Hoechst 33342 were purchased from Beyotime. Cy5 nucleic acid labeling kit was purchased from Mirus bio. Chlorpromazine, nystatin, amiloride were purchased from J&K Scientific. NBD-PE and Rh-PE, Lipofectamine 2000 were purchased from Thermo Fisher Scientific. Membrane fluidity assay kit was purchased from Abcam. EndoFree Maxi Plasmid Kit was purchased by Tiangen.

2.2. Synthesis of lipids

AD lipids were synthesized in three steps (Scheme S1). Firstly, AD-a was prepared. Oleic acid (10.0 g, 35.40 mmol) was dissolved in dichloromethane (DCM, 200 mL), which was added by 2-hydroxymethyl-1,3-propanediol (7.51 g, 70.80 mmol), 4-dimethylaminopyridine (DMAP) (0.43 g, 3.54 mmol), triethylamine (TEA) (5.37 g, 53.10 mmol), and *N*-(3-Dimethylaminopropyl)-*N*′-ethylcarbodiimide hydrochloride (EDCI) (10.13 g, 53.10 mmol), with stirring for 10 min under the ice bath. Then, the mixture was recovered to room temperature and stirred overnight. After successive washing with water, 10 % Citric acid aqueous solution, and brine, the mixture was then dried by using Na_2SO_4, following filtration and evaporation under vacuum. The residue was purified by silica gel chromatography (30 % ethyl acetate in hexanes) to give AD-a (8.38 g, 22.61 mmol, 63.88 %) as a colorless oil. Next, 1-adamantaneacetic acid (4.39 g, 22.61 mmol), DMAP (0.28 g, 2.26 mmol), TEA (3.43 g, 33.92 mmol), EDCI (6.47 g, 33.92 mmol) were added into the solution of AD-a (8.38 g, 22.61 mmol) in DCM (200 mL), and stirred for 10 min under the ice bath. After stirring overnight at room temperature, the mixture was washed in turn with water, 10 % citric acid aqueous solution, and brine. Then, the mixture was dried by using Na_2SO_4, filtered, and evaporated under vacuum. The residue was purified by silica gel chromatography (10 % ethyl acetate in hexanes) to give AD-b (8.56 g, 15.65 mmol, 69.22 %) as a colorless oil. Finally, various amine heads were reacted with AD-b to obtain the AD lipids from AD1 to AD8. In brief, AD-b (0.80 g, 1.46 mmol) was dissolved in DCM (20 mL), into which 4-nitrophenylchloroformate (0.53 g, 2.63 mmol), DMAP (0.18 g, 1.46 mmol), and TEA (0.30 g, 2.93 mmol) were added and stirred for 1 h under the ice bath. Then, different amine heads (7.31 mmol) and DMAP (0.18 g, 1.46 mmol) were added to the solution and stirred for 2 h, respectively. After in turn washing with water, 10 % citric acid aqueous solution, 5 % sodium hydroxide solution, and brine, the mixture was dried by using Na_2SO_4, filtered, and evaporated under vacuum. The residue was purified by silica gel chromatography (4 % MeOH in DCM) to give AD lipids as colorless oils.

The synthesis of PEG_{2000}-Suc-TA_2 included three steps (Scheme S2). In brief, TA_2-NH_2 was first synthesized. *L*-glutamate (1.00 g, 6.80 mmol) was dissolved in anhydrous toluene (30 mL), into which *p*-Toluenesulfonic acid (1.40 g, 8.16 mmol) was added for stirring at reflux for 2 h. The reaction was then cooled to room temperature, following the addition of 1-Tetradecanol (2.91 g, 13.59 mmol) for another stirring at reflux overnight. The reaction mixture was evaporated under reduced pressure to give a thick dark brown oil which was then dissolved in dichloromethane, washed with saturated sodium bicarbonate solution and brine in turn. After drying by using Na_2SO_4, the mixture was filtered and the filtrate was evaporated under vacuum. The residue was purified by silica gel chromatography (10 % ethyl acetate in hexanes) to obtain TA_2-NH_2 (1.93 g, 3.57 mmol, 52.60 %). Then, TA_2-COOH was synthesized. TA_2-NH_2 (0.50 g, 0.93 mmol) was dissolved in DCM (10 mL) with the addition of succinic anhydride (0.20 g, 2.00 mmol) and DMAP (0.25 g, 2.00 mmol) for stirring at reflux for 24 h. The reaction mixture was evaporated under reduced pressure to give a yellow solid. The residue was purified by silica gel chromatography (5 % MeOH in DCM) to give TA_2-COOH (0.43 g, 0.68 mmol, 72.89 %). Finally, TA_2-COOH (0.43 g, 0.68 mmol), EDCI (0.19 g, 1.00 mmol), DMAP (0.16 g, 1.31 mmol), *N*,*N*-diisopropylethylamine (DIPEA) (0.17 g, 1.32 mmol), $mPEG_{2000}$-OH (2.62 g, 1.31 mmol) were dissolved in DCM (20 mL) and stirred at room temperature for 24 h. The reaction mixture was evaporated under reduced pressure to give a yellow solid. The residue was purified by silica gel chromatography (4 % MeOH in DCM) to give PEG_{2000}-Suc-TA_2 (0.38 g, 0.14 mmol, 78.60 %) as a white solid.

The ^{1}H NMR (Bruker 300 or 500 MHz spectrometer) and HRMS (ESI) of all lipids were shown in supporting information.

2.3. Preparation and characterization of LNPs

For rough screening, LNPs were prepared by the ethanol injection method. Briefly, all lipids including ionizable lipid (TA7 or TA13), adamantane-containing lipid (AD1-AD8), DOPE, cholesterol, and PEG_{2000}-Suc-TA_2 at different mole ratios were dissolved in anhydrous ethanol, while PmaxGFP as the model pDNA was diluted in 10 mM citrate buffer (pH 4). The ethanol solution was added to triple volume of citrate buffer drop by drop. After mixing, the mixture was dialyzed against PBS buffer by using a 1.4 K MWCO (molecular weight cut-off) dialysis membrane for 2 h to gain the LNPs. In the process of optimizing the formulation, the pDNA concentration remained constant, while the ratio of PEG_{2000}-Suc-TA_2, the kind of neutral phospholipid (DSPC, DMPC, DPPE, DSPE, SPC, DOPC) and the N/P ratio were altered.

After fixing the top-performing formulation, the preparation method was further optimized by using a microfluidic device. One volume of lipid mixtures in ethanol and three volumes of pDNA solutions were

mixed by using syringe pump (Pump 11Elite, Harvard) to drive the solutions through the microfluidic device (Wenhao Microfluidic Technology) at a combined flow rate of 4 mL/min (1 mL/min for ethanol and 3 mL/min for aqueous buffer). The particle *Z*-average sizes and zeta potential of LNPs were measured by dynamic light scattering (NanoBrook Omni, Brookhaven). Agarose gel electrophoresis was utilized to evaluate the pDNA encapsulation efficiency. All samples containing with 200 ng of pDNA were loaded onto 0.7 % agarose gel for electrophoresis (130 V, 20 min). The gel was stained by Ultra GelRed and visualized on the gel imaging system (5200 Multi, Tanon).

McDNA-CD19-3NF/TA7AD8 LNPs were prepared by the best formulation and preparation method as above. In the best transfection manner, we co-encapsulated two plasmids of mcDNA-CD19-3NF and transposase at a ratio of 2:1 (*w*/w).

For transmission electron microscopy (TEM) imaging, 20 μL of LNPs were placed onto the carbon-coated 200 mesh Cu grid. Then, the sample was stained with 20 μL of 2 % phosphotungstic acid solution for 3 min. The excess solution was absorbed using filter paper. After drying, the morphology of LNP was observed by transmission electron microscope with an operating voltage of 100.0 kV (Hitachi, HT7700).

To evaluate the stability of top-performing LNP, TA7AD8 LNP diluted in PBS was stored at 4 °C for up to 60 days. At each time point, an aliquot was pulled from the sample to measure the particle size and polydispersity.

2.4. Isolation and culture of human primary $CD3^+$ T cells

Human peripheral blood mononuclear cells (PBMCs) were collected from healthy volunteer donors by density gradient centrifugation with human peripheral blood lymphocyte separation medium. All the experiments were performed in compliance with the Guide for Use of Human Blood, approved by the Ethics Committee of China Pharmaceutical University. All the donors had been informed before the experiments. After collection of the PBMC layer, the red blood cells were lysed by using RBC lysis buffer and washed with PBS twice. Then, $CD3^+$ T cells were isolated using the EasySep™ Human T Cell Isolation Kit according to the manufacturer's protocol and were then cultivated in T cell medium containing 100 IU/mL of recombinant human IL-2 and 25 μL/mL of ImmunoCult™ Human CD3/CD28 T cell activator.

2.5. In vitro transfection of pDNA-LNP into primary T cells

Human primary $CD3^+$ T cells were seeded at a density of 50,0000 cells per well in a 24-well plate. Then, 100 μL of LNP solution (containing 1 μg of pmax GFP) was added into each well for incubation of 48 h at 37 °C in a 5 % CO_2 incubator. The expression of GFP was monitored by inverted fluorescence microscopy (Nikon, Ts2R) and determined by flow cytometry (Attune NxT, Thermo Fisher). Lipofectamine 2000, a commercially available transfection reagent, was used as a positive control.

2.6. Culture and transfections of HeLa cells

To assess the gene expressions of mcDNA-CD19-3NF and pCD19-CAR, Hela cells were seeded in 24-well plates at 1×10^5 cells per well and grown to 80 % density prior to transfection. Lipofectamine 2000 was performed for transfection following the manufacturers' protocols. The expression of GFP was monitored by inverted fluorescence microscopy (Nikon, Ts2R) and determined by flow cytometry (Attune NxT, Thermo Fisher).

2.7. Calculation of encapsulation efficiency

The encapsulation efficiency of top-performing TA7AD8 LNP using the dsDNA HS Assay Kit. Briefly, Equal concentrations of lipid nanoparticles (LNPs) were divided into two groups: one treated with Triton X-100 to lyse particles and release total RNA, and the other left untreated to retain intact LNPs. After 5 min, the LNP samples and purified pDNA (0–20 μg/mL, for standard curve) were plated in a 96-well plate with three duplications. Fluorescent dsDNA reagent was added according to the manufacturer's instructions, and the generated fluorescence was measured on a microplate reader at Ex/Em = 480/520 nm. F_i for untreated LNPs and F_t for Triton X-100-lysed LNPs. Encapsulation efficiency (EE%) was calculated using the formula: $EE\% = (F_t\text{-}F_i)/F_t \times 100$ %. The final pDNA content was calculated based on the pDNA standard curve.

2.8. Toluene nitrosulphonic acid (TNS) assay

The apparent pK_a of LNPs were measured using the 6-(p-Toluidino)-2-naphthalenesulfonic acid (TNS) assays. Briefly, 5 μL of LNP solution (20 μM) and 5 μL of TNS solution (60 μg/mL) were added to 140 μL of buffer solution with different pH values from pH 2 to pH 12 at an increment of 0.5 in a 96-well plate and mixed well. The fluorescence intensity of each group was measured at excitation and emission wavelengths of 320 nm and 450 nm. The pK_a value was estimated as the pH corresponding to 50 % LNP protonation, assuming that minimum fluorescence represents zero charge and maximum fluorescence represents 100 % charge.

2.9. Cellular uptake assay

Cy5-labeled PmaxGFP (Cy5-PmaxGFP) was prepared by using the Cy5 nucleic acid labeling kit according to the manufacturer's protocol. Then, human $CD3^+$ T cells were seeded in a 24-well plate at 500,000 cells per well and incubated with Lipo2000/Cy5-pmaxGFP or LNP/Cy5-pmaxGFP at 37 °C for 6 h. Then, the cell culture medium was removed, and cells were washed with PBS twice. The nucleus was then stained by Hoechst 33342 (1: 1000, v: v) for 10 min, following the observation of cellular uptake by confocal laser scanning microscope (CLSM, Zeiss, LSM 880). Moreover, the intensity of Cy5 within T cells was detected by flow cytometry (Attune NxT, Thermo Fisher).

2.10. Endocytosis pathway evaluation

T cell culture media containing different uptake mechanism inhibitors were prepared, including: (1) chlorpromazine (20 μg/mL); (2) nystatin (15 μg/mL); (3) amiloride (133 μg/mL). T cells (5×10^5 cells per well in 24-well plate) were pre-incubated in T cell culture medium precooled to 4 °C or T cell culture medium containing different uptake mechanism inhibitors for 1 h. Then, the cells were incubated with LNP/Cy5-PmaxGFP for another 6 h. Then, the intensity of Cy5 within the cells was analyzed by flow cytometry (Attune NxT, Thermo Fisher).

2.11. Intracellular tracking study

Human $CD3^+$ T cells were seeded in 24-well plates at a density of 1×10^6 cells/mL and treated with LNP/Cy5-PmaxGFP for 6 h. Then, the cell culture medium was removed, and cells were washed with PBS twice and continued to incubate in fresh T cell medium for 0 h or 2 h. At different time points, T cells were stained with LysoTracker green and Hoechst 33342 at 37 °C for 15 min. After washing with PBS twice, T cells were re-suspended in PBS and added into laser confocal dish, followed by observation using CLSM (Zeiss, LSM 880).

To further demonstrate that LNPs leveraged the tubulin-mediated intracellular transport, human primary $CD3^+$ T cells were treated with LNP/Cy5-PmaxGFP for 2 h, T cells were stained with tubulin-tracker green, Hoechst 33342 at 37 °C for 15 min. After washing with PBS twice, T cells were re-suspended by T cell culture media and added into laser confocal dish, followed by observation using CLSM (STELLARIS5, Leica) for ultra-high-resolution imaging and real-time imaging.

2.12. Membrane fusion and fluidity assay

The membrane fusion ability of TA7AD8 LNP with lysosomal mimicking anionic liposomes was evaluated by fluorescence resonance energy transfer (FRET) assay. Lysosomal mimicking anionic liposomes were prepared by the film dispersion method with formulation of DSPC: DOPE: DOPS: Chol: NBD-PE: Rh-PE = 20: 20: 20: 15: 1: 1 (mol: mol), and total lipid concentration was fixed at 48 μM. TA7 LNP and TA7AD8 LNP solutions were diluted using citrate buffer (pH = 6.0 and 5.0) to fix total lipid concentration at 120 μM. Then, 120 μL of LNP was mixed thoroughly with 30 μL of Lysosomal mimicking anionic liposomes. After incubating at 37 °C for 5 min, fluorescence measurements (F) were conducted on microplate reader at Ex/Em = 480/538 nm. Only lysosomal mimicking anionic liposomes were set as a negative control (F_{min}). Lysosomal mimicking anionic liposomes incubated with 1 % Triton X-100 solutions were set as a positive control (F_{max}). The lipid fusion (%) was calculated as $(F - F_{min})/(F_{max} - F_{min}) \times 100$ %.

Membrane fluidity of LNP was assessed by using the Membrane Fluidity Kit. LNP solutions (TA7 LNP, TA7AD8 LNP) were labeled with lipophilic pyrene probe (10 μM pyrene decanoic acid and 1 % pluronic F-127 in PBS) for 1 h in the dark at room temperature with shaking. By measuring the ratio of Ex/Em = 350/400 nm and Ex/Em = 350/470 nm, a quantitative monitoring of the membrane fluidity was attained. Data are expressed as ratio between pyrene excimer and monomer. Data were normalized to TA7 LNP.

2.13. Molecular dynamic simulation

In this study, we compared the properties of two bilayer membrane systems. The first system comprised TA7, Chol, DOPE, and PEG_{2000}-Suc-TA_2 in a molar ratio of 36:48.5:15:0.5, while the second system included TA7, AD8, Chol, DOPE, and PEG_{2000}-Suc-TA_2 in a molar ratio of 18:18:48.5:15:0.5. Each system was constructed with 800 lipid molecules randomly arranged. We conducted three parallel 100 ns MD simulations on each of these two systems.

Our workflow began with conformational optimization for TA7, AD8, Chol, DOPE, and PEG_{2000}-Suc-TA_2 using GaussView6 along with Gaussian16, and calculated their corresponding RESP2 [19] charges with Multiwfn [20]. Subsequently, we generated structure files for these five molecules to serve as input files for molecular dynamics simulations using Sobtop. Each system was randomly assembled using genmixmem. After energy minimization and initial NPT ensemble equilibration, we performed 100 ns NPT ensemble simulations. The entire molecular dynamics simulations were conducted using GROMACS 2022.5 [21] and the AMBER14SB force field [22]. Figures were generated using VMD.

The Luzzati thickness [23] of two membrane systems was calculated using the Python library MDTraj [24], which is designed for analyzing MD trajectories. This involved subtracting the integral of the probability distribution of water molecules from the repeat spacing D.

The relative depth of water molecules infiltrated into the hydrophobic interior was calculated by the formula as

$$\%relative\ depth = \frac{(z2 - z1) + (z4 - z3)}{(z4 - z1)},$$

where z1, z4 correspond to the boundaries of the hydrophobic interior of the bilayer, respectively, and z2, z3 are the deepest positions at which water atoms penetrate the hydrophobic interior of the bilayer, respectively.

2.14. Generation of minicircle CD19-CAR plasmid (mcDNA-CD19-3NF)

Basic piggyBac transposon plasmid (pCD19-CAR) and transposase plasmid were entrusted to VectorBuilder for synthesis. pCD19-CAR is a polycistronic genetic construct that co-expresses enhanced green fluorescent protein (EGFP) and the CAR gene linked by a T2A peptide sequence. Thus, GFP could be used as surrogate marker for CAR-expression. Firstly, the 3NFs sequence, consisting of upstream (3NF1) and downstream (3NF2), were inserted into the basic vector plasmid pCD19-CAR by *Kpn*I and *Hind*III endonuclease. CD19-3NF DNA fragments, including CD19-CAR expression cassette, EGFP, and 3NFs, were generated by linearized pCD19-CAR with polymerase chain reaction (PCR) and added *Eco*RI and *Xab*I restriction sites to its 5′- and 3′-end. Linearizing pMC.BESPX-MCS2 plasmid (MN100B1 plasmid) in the same protocol. Then, we directionally ligated two linearized DNA fragments by T4 DNA ligase to generate the parental minicircle plasmid pMC.BESPX-CD19-3NF. Transformed *E. coli* carrying pMC.BESPX-CD19-3NF was cultured with TB medium containing 100 μg/mL kanamycin, with a rotation speed of 200 rpm at 37 °C overnight. To assist the generation of mcDNA-CD19-3NF, the expression of ΦC31 integrase and *Sce*I endonuclease was induced by adding the same volume LB medium, containing 10 % L-arabinose. After an additional 5.5 h cultivation with a rotation speed of 250 rpm at 30 °C, bacteria cells were harvested and mcDNA-CD19-3NF purified using TIANGEN's EndoFree Plasmid Maxi Kit. The correct sequence of gene sequences was verified by gene sequencing. Oligonucleotides and primers used for mcDNA-CD19-3NF were shown in Table S6.

2.15. Exploration of physiological functions of CD19 CAR-T cells

For cell apoptosis, human primary $CD3^+$ T cells were seeded at a density of 5×10^5 cells per well in a 24-well plate and treated with mcDNA-CD19-3NF/TA7AD8 LNP for 48 h at 37 °C. The cells were harvested, washed with PBS twice, and suspended in 100 μL of the binding buffer containing 2.5 μL of Annexin V-PE and 2.5 μL of 7-Aminoactinomycin D (7-AAD) for 10 min in the dark. The cells were immediately analyzed with flow cytometer mentioned above (Attune NxT, Thermo Fisher). Human primary $CD3^+$ T cells were transfected by Nucleofector Device (Nucleofector Device ™ System, Lonza) following the manufacturer's protocols as control.

For CAR expression, human primary $CD3^+$ T cells were seeded at a density of 5×10^5 cells per well in a 24-well plate and treated with mcDNA-CD19-3NF/TA7AD8 LNP. At each time point, the expressions of GFP were analyzed by flow cytometry.

To measure the phenotypical ratio of the generated CAR T cells, CD19 CAR-T cells were stained with APC anti-human CD4 antibody (0.5 μg/mL) and PE anti-human CD8 antibody (0.5 μg/mL), following the analysis by flow cytometry (Attune NxT, Thermo Fisher). Normal T cells were used as a control.

For proliferation assay, normal T cells, CD19 CAR-T cells were cultured for 10 days at 37 °C in a 5 % CO_2 incubator. The number of cells was calculated every other day, and the proliferation curve was generated.

2.16. Activation and exhaustion phenotype of CD19 CAR-T cells

Naive unmodified T cells and CD19 CAR-T cells were co-cultured with Raji cells at an effector-target (E: T) ratio of 5:1 on 24-well plates, respectively. After 24 h incubation, the cells were collected and stained separately with FITC anti-human CD3 antibody, PerCP/Cy5.5 anti-human CD69 antibody, APC anti-human TIM-3 antibody. CD19-CAR-T and Raji cells are distinguished based on the expression of CD3. The expression of the early T cell activation markers CD69 and T cell exhaustion markers were quantified by flow cytometry (Attune NxT, Thermo Fisher).

2.17. The effector function of CD19 CAR-T cells

Naive unmodified T cells and CD19 CAR-T cells were co-cultured with Raji cells at an effector-target (E:T) ratio of 5:1 on 24-well plates, respectively. After 24 h incubation, the cells were collected and stained separately with FITC anti-human CD3 antibody. Next, cells were fixed

with 4 % paraformaldehyde (PFA) and permeabilized using 0.1 % Triton X-100. After that, cells were stained with PE/Cy7 anti-human/mouse GZM B antibody (0.8 μg/mL), PE anti-human TNF-α antibody (0.8 μg/mL), and APC anti-human IL-2 antibody (0.8 μg/mL). Expressions of CD69, IL-2, GZM B, and TNF-α were quantified by flow cytometry (Attune NxT, Thermo Fisher).

2.18. Lactate dehydrogenase (LDH) cytotoxicity assay

Naive unmodified T cells and CD19 CAR-T cells were mixed with Raji cells at the ratio of 20:1, 10:1, 5:1, 1:1 in T cell medium. After 24 h, the cytotoxic efficiency was measured by quantifying the release of endogenous LDH from tumor cells using the LDH Cytotoxicity Assay Kit according to the instruction of the manufacturer. Briefly, the culture supernatant from cells were transferred to a new 96-well plate and mixed with LDH reaction mixture. After a 30 min of incubation at room temperature with shaking, the absorbance at 490 nm was measured by microplate reader (Synergy H1, Biotek) to determine LDH activity. Untreated T cells were used as a control.

2.19. Xenograft mouse models

NOD-SCID IL-2 receptor gamma null (NSG) mice were injected with 1×10^6 Raji-Luc cells via the tail vein to construct acute lymphoblastic leukemia models. After luciferase-induced fluorescence was observed (in approximately 5 days), tumor-bearing mice were randomly divided into 3 groups ($n = 5$ per group) and intravenous injected with PBS, CAR-T cells constructed by TA7AD8 LNP (2×10^6) and CAR-T cells constructed by lentivirus (2×10^6). Bioluminescence imaging was performed on the small animal in vivo imaging system (IVIS) after intraperitoneal injection of D-luciferin at 0.15 mg per g body weight, and the data were analyzed using Tanon system software.

At study termination (Day 15), major organs (Heart, liver, spleen, lung and kidney) were harvested and fixed in 4 % paraformaldehyde for 48 h. Tissues were paraffin-embedded, sectioned at 5 μm thickness, and stained with hematoxylin and eosin using standard protocols.

2.20. In vivo persistence and proliferation capacity of CD19 CAR-T cells

To assess the in vivo persistence of LNP-based CAR-T cells, peripheral blood (0.1 mL) was collected from tumor-bearing NSG mice at days 5, 10, and 15 post treatment. Erythrocyte depletion was performed using RBC lysis buffer (5 min incubation on ice). And then the cells were stained with APC anti-human CD3ε antibody (30 min at 4 °C) to identify human T cells. The proportion of CAR-T cells within the total $CD3^+$ T-cell population was quantified via flow cytometry (Attune NxT, Thermo Fisher).

2.21. Statistical analysis

All results were presented as the mean ± SD, unless otherwise noted. Statistical analysis was performed using GraphPad Prism 9.0 software. Statistical significance was analyzed by the unpaired *t*-test, one-way ANOVA or two-way ANOVA. (*p*-Value: ns or unmarked, not significant; $^*P < 0.05$, $^{**}P < 0.01$, $^{***}P < 0.001$, $^{****}P < 0.0001$).

3. Results and discussion

3.1. Design of functional lipids and construction of top-performing LNP for human primary T cells transfection

To improve the transfection effect of LNPs on T cells, we first designed a series of functional adamantane lipids consisting of a tertiary amine head, a biodegradable carbonate ester linker, and asymmetric tails which included a rigid adamantane tail for tropism to T cells and a flexible oleic acid tail for membrane fluidity (Fig. 1). These adamantane lipids were synthesized via a simple three-step esterification reaction, which was facile for future application (Scheme S1). All the adamantane lipids were characterized by using ^{1}H NMR, ^{13}C NMR, and HRMS (Figs. S1–17). Next, two ionizable lipids of TA7 and TA13 with an *N*-methyl pyrrolidine amine head, biodegradable glutamic acid ester linker, and two 1-tetradecanol tails were synthesized according to our previous report, which can effectively deliver siRNA into HeLa cells with high transfection efficiency [25], but fail to deliver pDNA into T cells. Besides, we synthesized a novel PEGylated lipid (PEG_{2000}-Suc-TA_2) holding the same tails with TA7 or TA13 through a simple esterification reaction (Fig. 1, Scheme S2), which was characterized by using ^{1}H NMR (Fig. S18).

In order to screen the top-performing LNP, we first determined the best combination of adamantane lipid and ionizable lipid for transfection of GFP pDNA into primary T cells. A series of LNPs composed of TA7 or TA13 as ionizable lipid, functional adamantane lipid (AD1-AD8), DOPE, cholesterol, and PEG_{2000}-Suc-TA_2 were prepared at a molar ratio of 18:18:15:48:1, which encapsulated the GFP pDNA at a N/P ratio of 7. The particle sizes and zeta potentials of these LNPs were shown in Tables S1 and S2. Interestingly, we found LNPs containing AD lipids exhibited smaller particle sizes (ranging from 150 to 170 nm) than those without AD lipids (ranging from 220 to 240 nm) (Fig. 2A), indicating that the ability of AD lipids to reduce the particle size of LNPs. Moreover, all the LNPs showed stable pDNA loading ability (Fig. S19a). We subsequently quantified the GFP expression in human primary $CD3^+$ T cells by using flow cytometry. Excitingly, LNPs with AD8 exhibited superior potential in delivering pDNA into human primary T cells, while other LNPs showed limited transfection efficiency which were lower than 1 % and similar to that of commercial Lipofectamine 2000 (Fig. 2B). These results further revealed the huge challenge in pDNA transfection into human primary T cells, and indicated the critical role of AD8 in promoting T cell transfection. Of which, TA7AD8 LNP showed the highest GFP-positive T cell ratios and the mean fluorescence intensity (MFI) of GFP.

Next, we optimized the LNP formulation including the kinds of neutral phospholipids, the ratio of PEGylated lipid, and the N/P ratio (Tables S3–5, Fig. S19b–g). Considering the pDNA loading stability and the transfection efficiency, we identified the top-performing LNP formulation of TA7, AD8, DOPE, cholesterol, and PEG_{2000}-Suc-TA_2 at a molar ratio of 18:18:15:48.5:0.5, N/P ratio of 7, the lipid concentration of 0.36 mg/mL, and the encapsulation efficiencies of 93.8 %. To gain higher transfection efficiency, the preparation technology was explored by using the microfluidic mixing method. We found that as the increase of flow rate, the particle size of TA7AD8 LNP gradually reduced from 150 nm to 60 nm (Fig. S20a). Moreover, different particle sizes resulted in varied transfection efficiency (Figs. 2C, D, and S20b). Thereinto, the smallest particle size of TA7AD8 LNP of about 60 nm achieved the highest transfection efficiency of about 18.3 % in human primary $CD3^+$ T cells, which was 3.5-fold and 25.8-fold higher than MC3 LNP, and Lipofectamine 2000, respectively (Fig. 2C). These data suggested that the uniform small size of LNP served as a key parameter for effective T cell transfection, probably improving the cellular uptake [26] and the subsequent lysosomal escape [27]. We finally examined the morphology of the top-performing TA7AD8 LNP by transmission electron microscopy (TEM), showing a uniform solid spherical shape of about 60 nm (Fig. 2E). Notably, after 4 weeks of storage at 4 °C, there were no obvious changes in particle size, PDI, the amount of DNA, and encapsulation efficiency of TA7AD8 LNP (Fig. S20c and d), indicating superior stability.

3.2. Top-performing TA7AD8 LNP improve cellular uptake and lysosomal escape

Then, we wondered about the underly reason for TA7AD8 LNP holding the high transfection efficiency. Thus, the cellular uptake, endocytic pathways, and the following endo/lysosomal escape that are

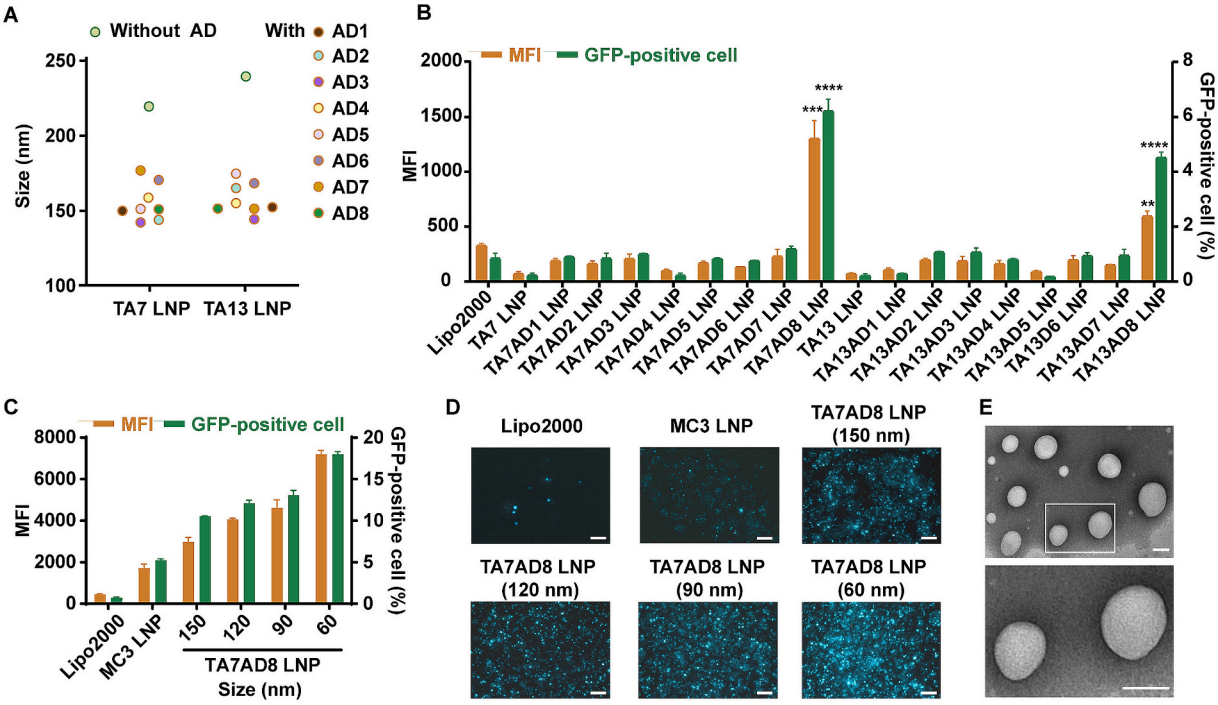

Fig. 2. Optimization and characterization of top-performing LNP. (A) Particle sizes of TA7 or TA13 LNPs with or without AD lipids. (B) The GFP expression of human primary $CD3^+$ T cells after treatment with various LNPs for 48 h at a dose of 1 μg/500000 cells by flow cytometry ($n = 3$, mean ± SD, Two-way ANOVA analysis, $^{**}P < 0.01$, $^{***}P < 0.001$, $^{****}P < 0.0001$). (C) The GFP expression of human primary $CD3^+$T cells after transfection by TA7AD8 LNPs with different particle sizes measured by flow cytometry. Lipofectamine 2000 and MC3 LNPs were used as controls (n = 3, mean ± SD). (D) The GFP expression of human primary $CD3^+$T cells after transfection by TA7AD8 LNPs with different particle sizes were observed by inverted fluorescence microscope. Lipofectamine 2000 and MC3 LNPs were used as controls. Scare bars: 100 μm. (E) TEM image of TA7AD8 LNP (60 nm, up), of which the white frame was enlarged (down). Scare bars: 50 nm.

closely related to the transfection efficiency of LNPs were explored [28]. We found that, after incubation with T cells for 6 h, TA7AD8 LNP encapsulating Cy5-labeled GFP pDNA resulted in a 99.7 % positive rate of $Cy5^+$ T cells, while that of Lipofectamine 2000 and TA7 LNP were only 66.3 % and 55.3 %, respectively (Fig. 3A). Moreover, the MFI of Cy5 treated with TA7AD8 LNP showed approximately 10-fold and 64-fold higher than that of Lipofectamine 2000 and TA7 LNP, respectively, which was further confirmed by the brightest Cy5 fluorescence within T cells by using confocal microscopy imaging (CLSM) (Fig. 3B). Furthermore, we compared the cellular uptake of TA7AD8 LNPs with different particle sizes in human $CD3^+$ T cells. The quantitative analysis demonstrated that while the positive rate of $Cy5^+$ T cells remained consistently high (>99 %) in all particle size groups, the MFI of Cy5 showed a significant size-dependent increase. Specifically, smaller-sized LNPs exhibited substantially higher MFI values compared to their larger counterparts, indicating enhanced cellular internalization efficiency with decreasing particle size (Fig. S21). These data indicated that the engagement of AD8 lipid in LNPs and the reduction of particle size obviously promoted the cellular uptake by T cells, conquering the first challenge faced by LNP transfecting T cells.

Notably, TA7 LNP exhibited limited cellular uptake in T cells (Fig. 3A), which precluded meaningful analysis of the endocytic pathway and downstream intracellular processes such as lysosomal escape. Next, we explored the endocytic pathway of TA7AD8 LNP by T cells which pretreated with chloropromazine, nystatin, or amiloride, the respective inhibitors of clathrin-mediated endocytosis, caveolae-mediated endocytosis or micropinocytosis [25]. For TA7AD8 LNP, all the inhibitors dramatically reduced the cellular uptake of TA7AD8 LNP (Fig. 3C), indicating that multiple endocytic pathways were involved in the endocytosis of TA7AD8 LNP, which might be one of the reasons for its high uptake by T cells. After endocytosis, the intracellular transport of TA7AD8 LNP within T cells was monitored by CLSM. After incubation with T cells for 6 h, we found the obvious co-localization of the Cy5-pDNA (red) and lysosomes labeled by Lyso-tracker green (green), indicating that pDNA-TA7AD8 LNP entered lysosomes after endocytosis. After LNP removal for another 2 h, the co-localization of Cy5-pDNA with lysosomes gradually disappeared, while the red Cy5-pDNA accumulation around the nucleus and entering into the nucleus stained by Hoechst 33342 (blue) (Fig. 3D and Fig. S22). Moreover, we confirmed that TA7AD8 LNP could leverage the tubulin-mediated intracellular transport by ultra-high-resolution confocal microscope image (Fig. 5E) and real-time imaging (Supplementary Video), exhibiting the transport tendency from the membrane site to the perinuclear site. The enhanced accumulation of pDNA around the nucleus might improve the entrance of pDNA into the nucleus due to the reduced movement distance in the cytosol. These data validly confirmed that TA7AD8 LNP could effectively enter the T cells, escape from the lysosomes, accumulate near the nucleus, and finally enter the nucleus to take effect.

To gain mechanistic insight into effective lysosomal escape, we explored the apparent pK_a of LNP which directly affected the surface charge of LNP at various pH environments and thus the interaction between LNP and membrane [29]. The apparent pK_a of TA7AD8 LNP showed about 5.4 by 6-(p-toluidinyl)naphthalene-2-sulfonic acid (TNS) assay [30], which was different from optimal pK_a (about 6–7) for siRNA or mRNA delivery [31]. Because LNP with low pK_a was able to remain in the early endosomes and escape from the lysosomes closer to the nucleus, circumventing the tough movement in the cytosol, which benefit the plasmid transfection. Additionally, a fluorescence resonance energy transfer (FRET) assay was applied to evaluate the ability of TA7AD8 LNP to fuse with and thus disrupt the lysosomal membrane (Fig. S23a). In brief, N-(7-nitrobenz-2-oxa-1,3-diazol-4-yl)-1,2-dihexadecanoyl-sn-glycero-3-phosphoethanolamine (NBD-PE) and Rhodamine B 1,2-dihexadecanoyl-sn-glycero-3-phosphoethanolamine (Rh-PE) were incorporated into liposomes as mimic lysosomes, in which the fluorescence of NBD was quenched by Rho due to the close distance. Once membrane fusion occurred, the NBD fluorescence rose owing to the increased

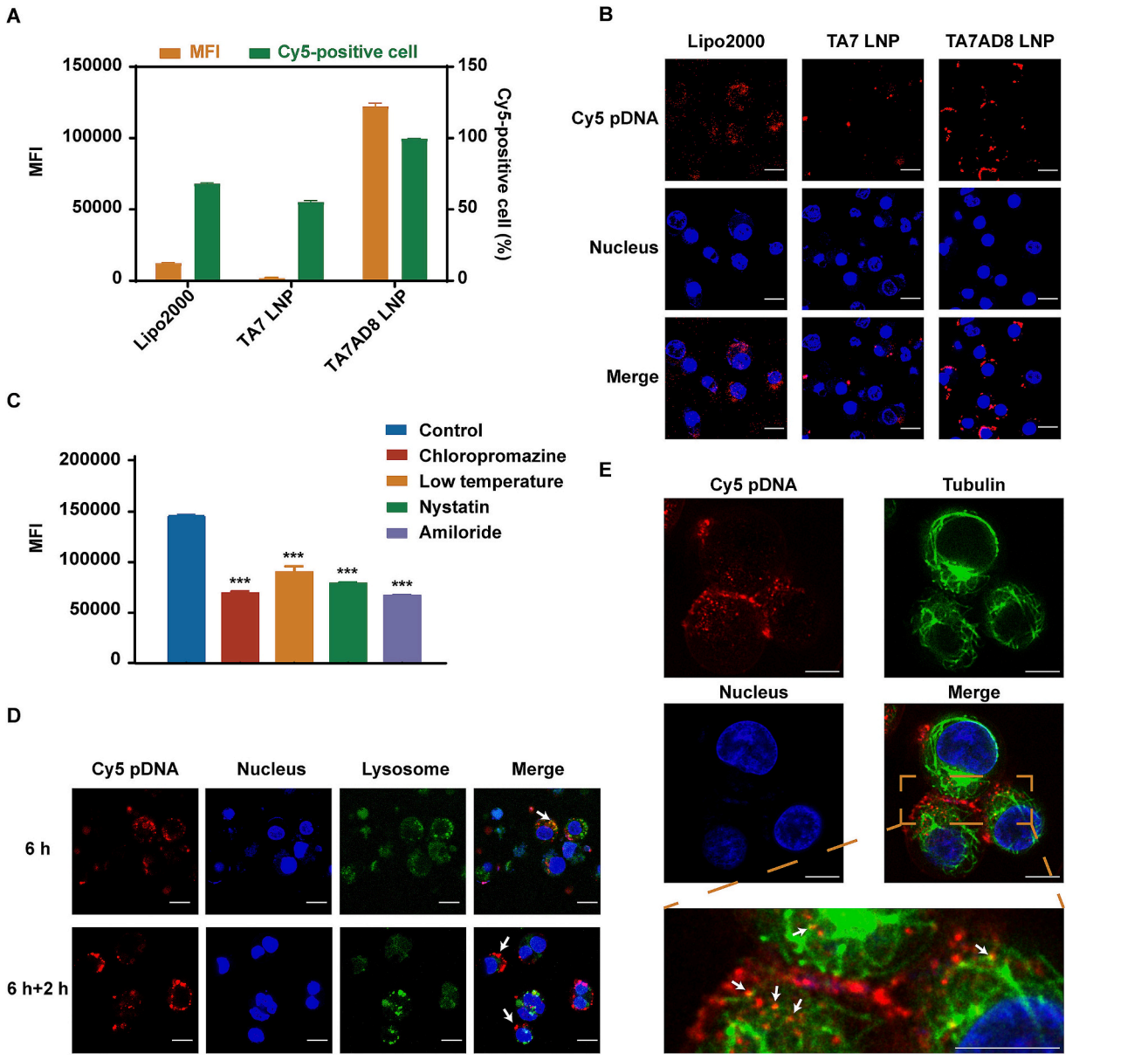

Fig. 3. Cellular uptake and the following intracellular transport of TA7AD8 LNP (60 nm) by human primary CD3$^+$T cells. (A) Cellular uptake of TA7AD8 LNP, TA7 LNP, and Lipofectamine 2000 were determined by flow cytometry (Mean ± SD, $n = 3$, Two-way ANOVA analysis, $^{****}P < 0.0001$). (B) CLSM images of human primary CD3$^+$T cells transfected with TA7AD8 LNP, TA7 LNP, and Lipofectamine 2000 at 6 h. pDNA was labeled by Cy5 (red) and the nucleus was labeled by Hoechst 33342 (blue). Scale bar: 10 μm. (C) Endocytic pathways of TA7AD8 LNP in human primary CD3$^+$T cells determined by flow cytometry (Mean ± SD, n = 3, One-way ANOVA analysis, $^{***}P < 0.001$). (D) CLSM images of lysosomal escape of TA7AD8 LNP within human primary CD3$^+$T cells at 6 h and 8 h. pDNA was labeled by Cy5 (red), the nucleus was labeled by Hoechst 33342 (blue), and lysosome was labeled by lysotracker green (green). Scale bar: 5 μm. (E) Ultra-high-resolution confocal microscope images of the tubulin-mediated transport of TA7AD8 LNP within human primary CD3$^+$T cells at 2 h. pDNA was labeled by Cy5 (red), tubulin was labeled by tubulin-tracker (green), and nucleus was labeled by Hoechst 33342 (blue). Scale bar: 5 μm. (For interpretation of the references to color in this figure legend, the reader is referred to the web version of this article.)

distance between the two probes [32]. Compared to TA7 LNP, TA7AD8 LNP exhibited stronger membrane fusion at pH 5.0. Especially, TA7AD8 LNP has stronger membrane fusion ability at pH 5.0 than at pH 6.0, indicating that TA7AD8 LNP could remain in endosomes and escape from the lysosomes (Fig. S23b). Further, we demonstrated the potentiated fluidity of TA7AD8 LNP by using the membrane fluidity kit (Fig. S23c) [33], which probably led to the improved membrane fusion. These data demonstrated the significance of AD8 lipid in promoting lysosomal escape via effective membrane fusion.

Taken together, TA7AD8 LNP addressed the challenges of cellular uptake and lysosomal escape, and further promoted the possibility of encapsulated pDNA into nucleus via the tubulin-mediated intracellular transport to circumvent the tough movement in viscous cytosol.

3.3. *Molecular dynamics simulation demonstrating the critical role of AD8 lipid in promoting LNP transfection*

To further explore the action of AD8, molecular dynamics (MD) simulations were performed. Firstly, we wondered about the reason for AD8 reducing the particle size of TA7AD8 LNP as compared to TA7 LNP. As detected by MD simulation, the bilayer thickness of the TA7AD8 bilayer was 2.82 nm, which was lower than that of the TA7 bilayer (3.02 nm). The thinner bilayer may be the reason that the addition of AD8 reduced the particle size, which is consistent with the previous report

that bilayer thickness affects the particle size distribution, and reducing them will reduce particle size [34]. Subsequently, we explored the promotion effect of AD8 on membrane fusion. The membrane lipid packing defects are identified as those regions in the outer leaflet where the packing of the hydrophilic lipid head groups is imperfect and the hydrophobic lipid tails are exposed to the aqueous environment. Some studies have shown lipid packing defects can promote membrane fusion by reducing the energy barrier [35,36]. We hypothesized that the addition of AD8 might enlarge the lipid packing defects of LNP. To confirm this, we quantified the number of atoms of all water molecules within 3 Å around the hydrophobic tail to characterize the lipid packing defect by using MD simulation, with more atoms indicating larger lipid packing defects. As expected, more water atoms in TA7AD8 bilayer indicated more lipid packing defects in three separate simulations, compared to TA7 bilayer (Figs. 4A and S24), as further confirmed by the top views of TA7AD8 bilayer showing larger blue areas than that of TA7 bilayer (Fig. 4B). Moreover, we plotted the density profiles of water atoms and hydrophobic atoms in TA7AD8 or TA7 bilayers (Fig. 4C), and calculated the relative depth of water molecules infiltrated into the hydrophobic interior that in TA7AD8 bilayer was 56.00 %, which was larger than that in TA7 bilayer, of only 49.07 %, indicating that the addition of TA8 resulted in a deeper lipid packing defect.

All MD data further verified the crucial roles of AD8 engagement, including reducing the particle size and improving the membrane fusion ability of LNP, which promoted the cellular uptake and lysosomal escape as well as the ultimate potentiated transfection efficiency of primary T cells by TA7AD8 LNP.

3.4. Construction and characterization of CD19 CAR-T cells via minicircle nuclear location transposon-encapsulated TA7AD8 LNP

The entry of pDNA, especially the large transposon system, into the nucleus is the final bottleneck in transfection of primary T cells. Therefore, we remolded the conventional PB transposon (pCD19-CAR, 7824 bp) through inserting an optimized DNA nuclear targeting sequence of 3NFs to enhance the nuclear import by interacting with the transcription factor [37], and then deleting the excess antibiotic sequences via using a minicircle backbone to reduce the size of transposon and enhance cell viability [38], resulting in the creation of minicircle nuclear location transposon (mcDNA-CD19-3NF, 5235 bp) (Fig. 5A).

The correct sequence was confirmed by Sanger sequencing and gel electrophoresis (Figs. S25 and S26), and the detailed map of mcDNA-CD19-3NF is shown in Fig. S27. Subsequently, we first assessed the transfection effect of modified transposons in model HeLa cells by using Lipofectamine 2000 (Fig. S28). The results showed that after the insertion of nuclear localization signal, the CAR expression enhanced and further increased with the aid of deleting the unnecessary sequences, indicating the necessity of both modifications. Then, the modified transposons were further evaluated in T cells by LNPs. It could be found that mcDNA-CD19-3NF exhibited obvious nuclear localization effect following 8-hour co-incubation with different LNPs, while pCD19-CAR-3NF showed no improved nuclear localization effect compared to pCD19-CAR (Fig. S29). These results indicated that NLS insertion alone was insufficient for effective nuclear localization in T cells due to the large size restricting the entrance into the nucleus. Thus, we only explored the transfection effect of mcDNA-CD19-3NF in the following studies.

Next, we applied TA7AD8 LNP to co-deliver mcDNA-CD19-3NF and transposase pDNA (mcDNA-CD19-3NF/LNP, encapsulation efficiencies of 91.4 %) into $CD3^+$ primary T cells in an optimized manner (Fig. S30), resulting in 10.8 % of CAR^+ T cells by quantified the GFP expression using flow cytometry (Fig. 5B), while pCD19-CAR/LNP only resulted in a 0.97 % of CAR^+ T cells, verifying the necessary of modified transposon in transfection efficiency. Moreover, the CAR expression was sustained

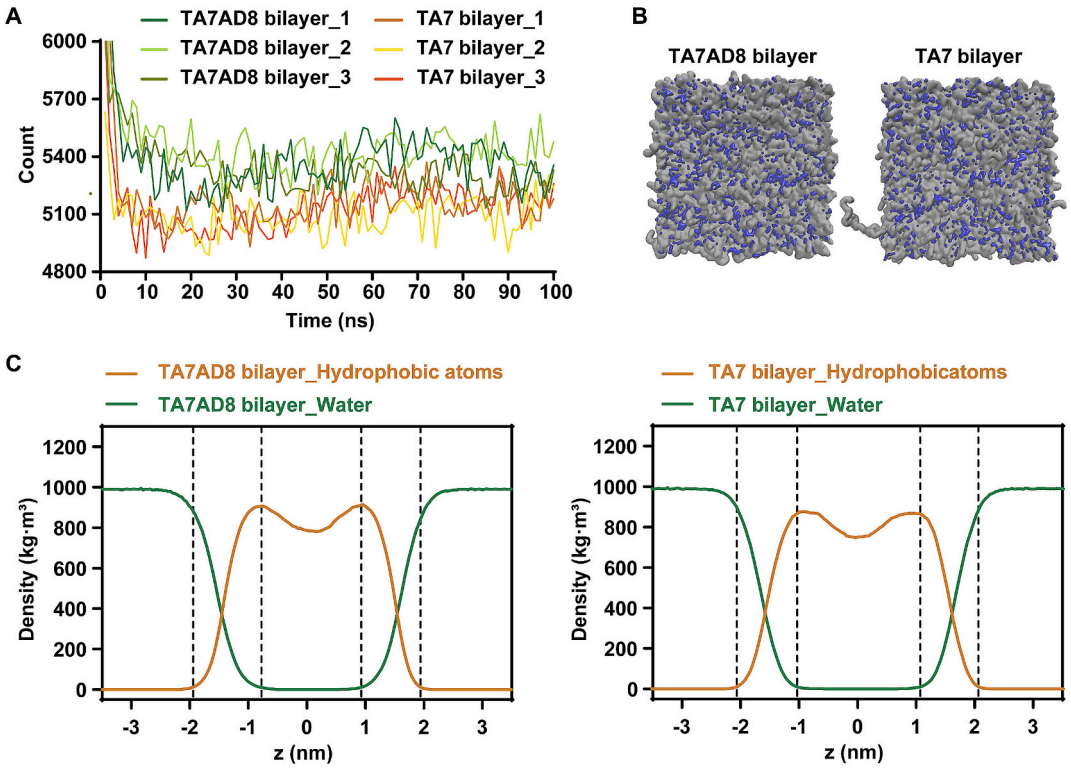

Fig. 4. Exploration of lipid packing defects by MD simulations. (A) The number of atoms of all water molecules within 3 Å around the hydrophobic tail in TA7AD8 or TA7 bilayer ($n = 3$). (B) Top views of TA7AD8 and TA7 bilayers in MD simulations. Lipid packing defects were represented by the water atoms within 3 Å around the hydrophobic tail (blue). (C) The density profiles for TA7AD8 or TA7 bilayer with the density of the whole hydrophobic atoms in green and water in orange. (For interpretation of the references to color in this figure legend, the reader is referred to the web version of this article.)

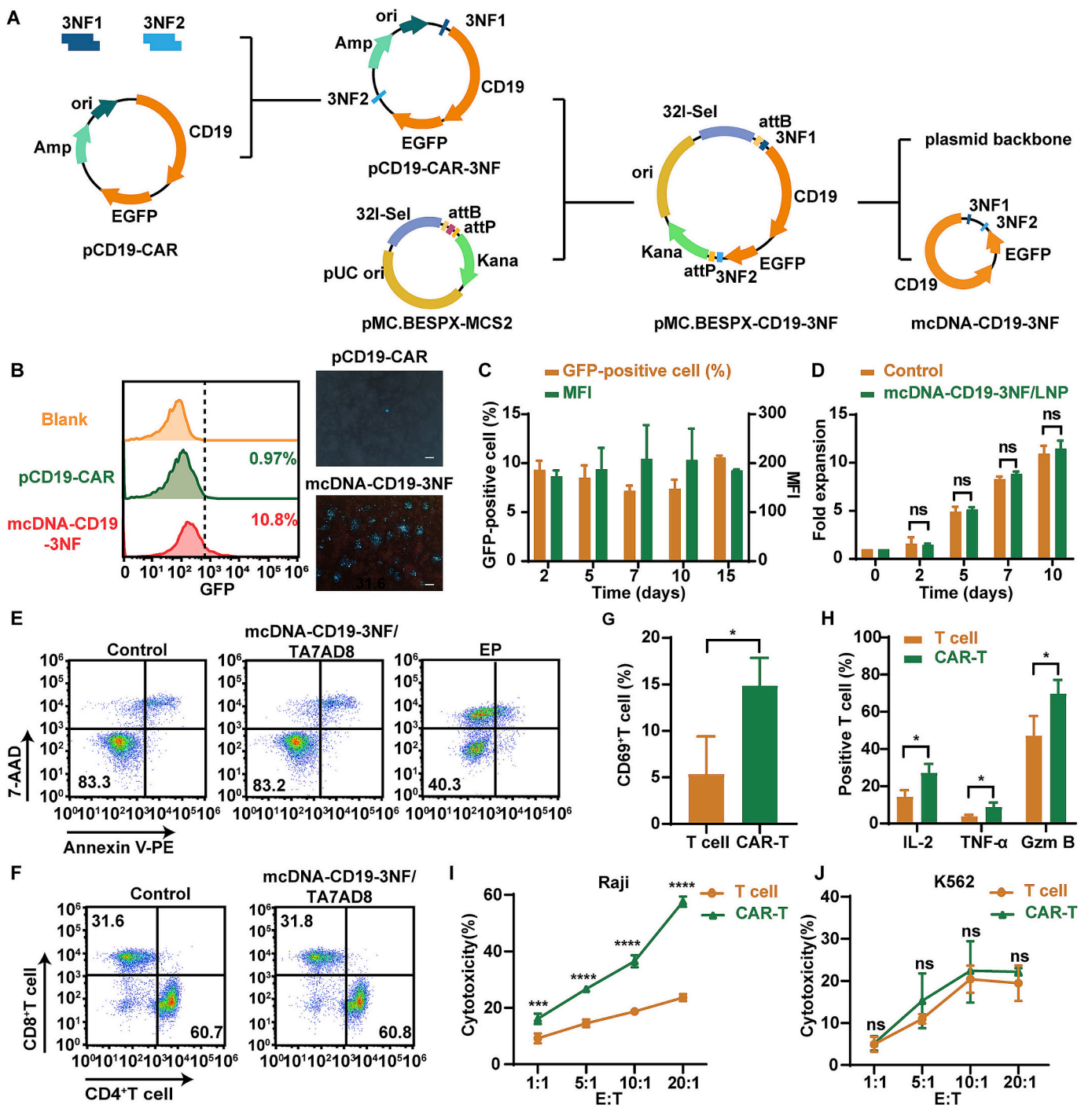

Fig. 5. Construction and characterization of CD19 CAR-T cells via mcDNA-CD19-3NF-encapsulated TA7AD8 LNP. (A) Schematic diagram of mcDNA-CD19-3NF generation. (B) Representative plots of CAR-CD19 expression (EGFP expression) after transfection of primary human T cells with mcDNA-CD19-3NF/TA7AD8 LNP and pCD19-CAR/TA7AD8 LNP for 48 h. Scare bars: 100 μm. The physiological functions of human primary $CD3^+$T cells after transfection by mcDNA-CD19-3NF/TA7AD8 LNP including: (C) expressions of CD19 CAR as time went, (D) cell proliferation ability, (E) cell apoptosis, (F) $CD4^+/CD8^+$ phenotype. (G) Flow cytometry analysis of expression of CD69 of CAR-T cells after co-culture with tumor cells ($n = 3$, two-tailed unpaired *t*-test, $^*P < 0.05$, $^{**}P < 0.01$). (H) Flow cytometry analysis of cytokine expressions (IL2, GZM B, TNFα) of CAR-T cells after co-culture with tumor cells (n = 3, mean ± SD, two-tailed unpaired *t*-test, $^*P < 0.05$, $^{**}P < 0.01$). (I, J) Tumor-killing ability of CD19 CAR-T cells against CD19-positive tumor cells (I) or CD19-negative tumor cells (J) after co-culture for 24 h at different effector-target (E: T) ratios. T cells were used as a control. (Mean ± SD, n = 3, Two-way ANOVA analysis, $^{***}P < 0.001$, $^{****}P < 0.0001$).

for at least 15 days, indicating that the transposon system integrated the CAR gene into the genome through a cut-and-paste mechanism (Fig. 5C).

Furthermore, the key physiological functions of CD19 CAR-T cells produced by mcDNA-CD19-3NF/LNP that are crucial to their efficacy were explored. We found that the proliferation, viability, and the ratio of $CD4^+/CD8^+$ cells of CD19 CAR-T cells were consistent with that of T cells (Fig. 5D–F), suggesting that TA7AD8 LNP would not change the cell viability and phenotype. Notably, CAR-T cells transfected by TA7AD8 LNP showed significantly reduced cytotoxicity compared to by electroporation (Fig. 5E), implying the superiority of transfection via LNP. Further, the level of CD69, a typical T cell activation marker, was

upregulated when exposed to CD19-positive target cells, indicating a specific activation of CD19 CAR-T cells constructed via TA7AD8 LNP upon antigen binding (Fig. 5G). Similarly, the expressions of interleukin-2 (IL-2), granzyme B (GZM B), and tumor necrosis factor-alpha (TNF-α) within CD19 CAR-T cells showed higher levels than T cells (Fig. 5H), further confirming the activation of CD19 CAR-T cells when recognizing the target cells. Finally, we showed that the constructed CD19 CAR-T cells effectively killed CD19-positive Raji cells (Burkitt's Lymphoma) rather than CD19-negative K562 cells (human chronic myeloid leukemia), especially at a high effector-to-target ratio (E:T = 20:1), indicating a specific killing upon antigen binding of CD19 (Fig. 5I and J). Meanwhile, CAR-T cells constructed by mcDNA-CD19-3NF/LNP showed similar cytotoxicity against tumor cells with those constructed by the lentivirus vector (Fig. S31). Our results demonstrated the efficacy and clinical potential of CAR-T cells produced by mcDNA-CD19-3NF/LNP.

3.5. *In vivo antitumor efficacy and safety evaluation of CD19 CAR-T cells constructed by TA7AD8 LNP*

Finally, to evaluate the in vivo antitumor potency and safety of CD19 CAR-T cells constructed by LNP, we established a xenograft model via intravenous injection of luciferase-expressed Raji cells (Raji-luci) into immunodeficient NOD-SCID IL-2 receptor gamma null (NSG) mice. On Day 5 post-tumor inoculation, mice were randomized into three groups: (1) PBS (negative control), (2) CAR-T cells constructed by TA7AD8 LNP (CAR-T (LNP)), and (3) CAR-T cells constructed by lentivirus (CAR-T (Lenti) group). Tumor progression was monitored by using the in vivo imaging system (IVIS) every 5 days. We found that CAR-T cells constructed by TA7AD8 LNP exhibited robust antitumor potency, achieving significant suppression of tumor growth compared to the PBS group (Fig. 6A and B). Moreover, the therapeutic efficacy of LNP-based CAR-T cells was comparable to that of lentivirus-produced CAR-T cells

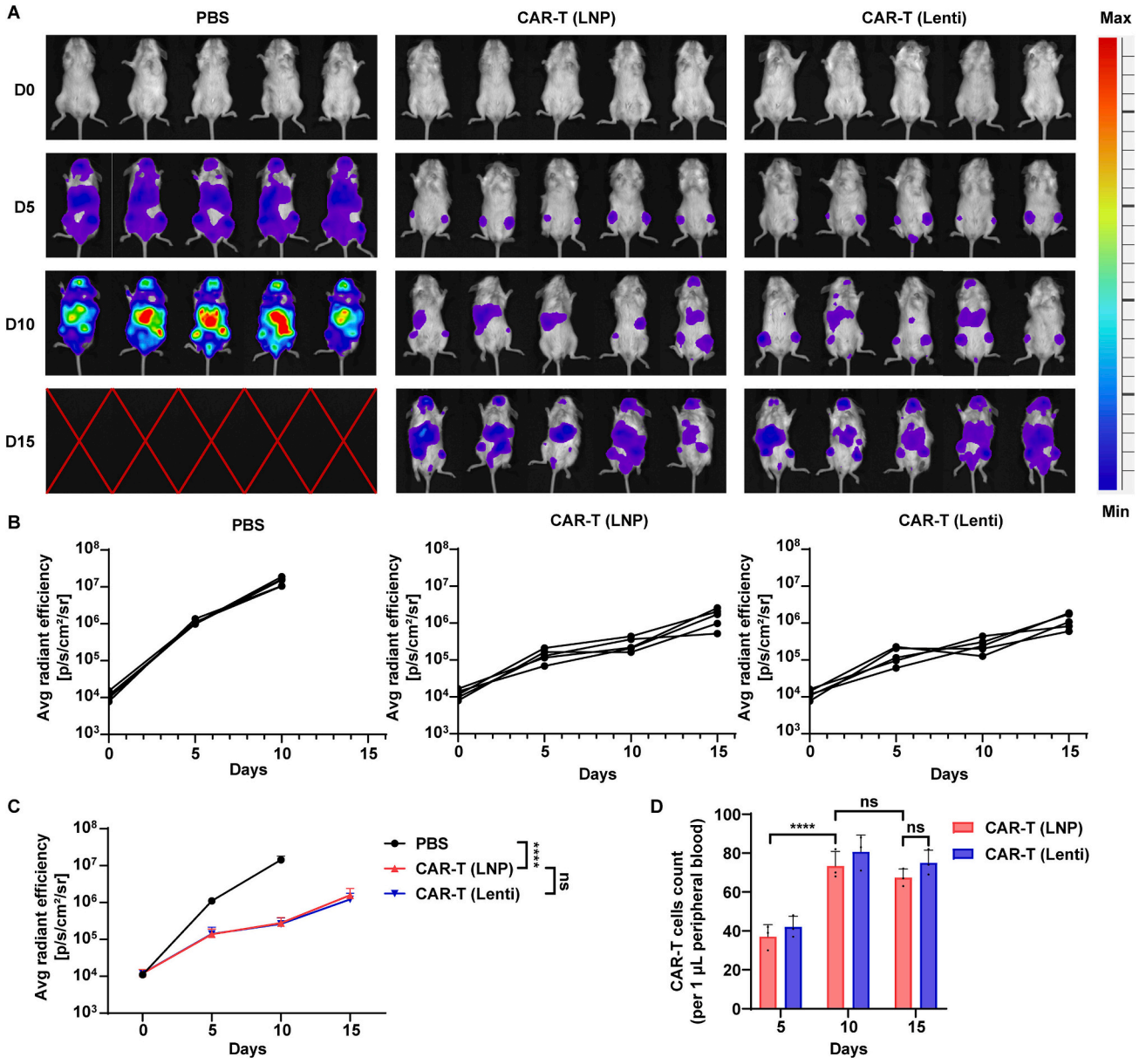

Fig. 6. In vivo antitumor efficacy of CD19 CAR-T cells constructed by TA7AD8 LNP. (A) The bioluminescence images of individual mice at the indicated time points. (B) Quantification of bioluminescence intensity of individual mice at the indicated time points. (C) Quantification of bioluminescence intensity of each group at the indicated time points. ($n = 5$, Two-way ANOVA with no matching, $^{****}P < 0.0001$, ns meant not significant). (D) Flow cytometry analysis of the proportion of CAR-T cells among $CD3^+$ T cells in peripheral blood at the indicated time points ($n = 3$, Two-way ANOVA with no matching, ns meant not significant).

(Fig. 6C), further demonstrating the effectiveness of LNP-transfected CAR-T cells.

The persistence and expansion of CAR-T cells in vivo are critical for effective leukemia treatment [39]. To evaluate the in vivo persistence of CAR-T cells constructed by TA7AD8 LNP, peripheral blood samples were collected on Days 5, 10, and 15 after administration to quantify the CAR-T cell populations via flow cytometry. On day 10, the CAR-T (LNP) group exhibited significantly higher peripheral CAR-T cell counts than on Day 5, with comparable levels sustaining through Day 15, suggesting continuous expansion of LNP-based CAR-T cells within the first 10 days after administration (Fig. 6D). Moreover, the expansion tendency of CAR-T cells produced by LNP was similar to that by lentivirus, indicating the comparable proliferating activity of LNP-based CAR-T cells with lentivirus-based CAR-T cells (Fig. 6D).

In addition, we demonstrated that mice in LNP-based CAR-T cells maintained the body weight which was attributed to the delayed tumor progression by the efficacy of CAR-T cells, while that of the PBS group decreased significantly along with uncontrolled disease progression (Fig. S32). Meanwhile, no significant toxicity was observed in mice treated with LNP-based CAR-T cells through hematoxylin and eosin (H&E) staining of sections of major organs (Fig. S33).

In short, we confirmed that CAR-T cells produced by LNP held the capability of expansion and robust antitumor potency in vivo, with clinical potential in the future.

4. Conclusions

In summary, we successfully constructed CD19 CAR-T cells with a 10.8 % of long-lasting CAR expression via a non-classical TA7AD8 LNP delivering minicircle nuclear location transposon into primary human $CD3^{+}$T cells, which sequentially conquered the challenges of cellular uptake, lysosomal escape, and transposon expression in the nucleus. Of which, the engagement of AD8 promoted the cellular uptake of LNPs by T cells due to the reduced particle size, as well as the potentiated lysosomal escape via improving membrane fluidity, inducing more lipid packing defects, and therefore enhancing membrane fusion. Interestingly, we found that the pK_a of TA7AD8 LNP for effective pDNA delivery was 5.4, probably because the lower pK_a led to LNP escaping from lysosomes which were closer to the nucleus, thus improving the probability of pDNA entering the nucleus. Furthermore, we proposed a promising method to remold transposons, which could be applied in other CAR transposons. Finally, we demonstrated that LNP-based CAR-T cells achieved antitumor efficacy comparable to lentivirus-generated CAR-T cells in the xenograft model, while demonstrating favorable safety profiles through H&E staining. This study provides a safe and valid tool for constructing gene-engineered human primary T cells with cost-effectiveness, which has a great perspective in the future.

Supplementary data to this article can be found online at https://doi.org/10.1016/j.jconrel.2025.113779.

CRediT authorship contribution statement

Mengtong Wu: Writing – original draft, Methodology, Conceptualization. **Jingwen Li:** Writing – original draft, Investigation, Data curation. **Yazhou Xu:** Software, Methodology. **Shaoxiong Lv:** Visualization, Validation. **Guan Wang:** Visualization, Software. **Yingshuang Huang:** Validation, Methodology. **Yu Tao:** Validation, Methodology. **Caoyun Ju:** Writing – review & editing, Supervision, Funding acquisition. **Can Zhang:** Supervision, Project administration, Funding acquisition.

Declaration of competing interest

The authors declare no conflicts of interest.

Acknowledgments

This work was supported by the National Natural Science Foundation of China (82130102, 92159304, 81930099, 82073785), the Natural Science Foundation of Jiangsu Province (BK20212011), the “Open Competition to Select the Best Candidates” Key Technology Program for Nucleic Acid Drugs of NCTIB (Grant No. NCTIB2022HS01014), “Double First-Class” University project (CPU2022QZ05), National Major Scientific and Technological Special Project for “Significant New Drugs Development” (2019ZX09301163), and the Open Project of State Key Laboratory of Natural Medicines (China Pharmaceutical University, SKLNMZZ202310). The authors thank Prof. Wenbin Shen and Dr. Hui-Min Xu of the Public Laboratory Platform at China Pharmaceutical University for assistance with NMR techniques.

Data availability

Data will be made available on request.

References

[1] S. Frantz, Engineered T-cell therapy shows efficacy in blood cancer, Nat. Biotechnol. 29 (2011) 853–855.
[2] G. Schett, A. Mackensen, D. Mougiakakos, CAR T-cell therapy in autoimmune diseases, Lancet 402 (2023) 2034–2044.
[3] J.G. Rurik, I. Tombacz, A. Yadeg, P.O. Mendez Fernandez, S.V. Shewale, T. Kimura, et al., CAR T cells produced in vivo to treat cardiac injury, Science 375 (2022) 91–96.
[4] G.I. Ellis, N.C. Sheppard, J.L. Riley, Genetic engineering of T cells for immunotherapy, Nat. Rev. Genet. 22 (2021) 427–447.
[5] L. Raes, S.C. De Smedt, K. Raemdonck, K. Braeckmans, Non-viral transfection technologies for next-generation therapeutic T cell engineering, Biotechnol. Adv. 49 (2021) 107760–107782.
[6] Y. Seow, M.J. Wood, Biological gene delivery vehicles: beyond viral vectors, Mol. Ther. 17 (2009) 767–777.
[7] A. Moretti, M. Ponzo, C.A. Nicolette, I.Y. Tcherepanova, A. Biondi, C.F. Magnani, The past, present, and future of non-viral CAR T cells, Front. Immunol. 13 (2022) 867013–867037.
[8] N. Nishio, R. Hanajiri, Y. Ishikawa, M. Murata, R. Taniguchi, M. Hamada, et al., A phase I study of CD19 chimeric antigen receptor-T cells generated by the PiggyBac transposon vector for acute lymphoblastic leukemia, Blood 138 (2021) 3831–3832.
[9] M.M. Billingsley, N. Singh, P. Ravikumar, R. Zhang, C.H. June, M.J. Mitchell, Ionizable lipid nanoparticle-mediated mRNA delivery for human CAR T cell engineering, Nano Lett. 20 (2020) 1578–1589.
[10] K. Syama, Z.J. Jakubek, S. Chen, J. Zaifman, Y.Y.C. Tam, S. Zou, Development of lipid nanoparticles and liposomes reference materials (II): cytotoxic profiles, Sci. Rep. 12 (2022) 18071–18081.
[11] M. Verma, I. Ozer, W. Xie, R. Gallagher, A. Teixeira, M. Choy, The landscape for lipid-nanoparticle-based genomic medicines, Nat. Rev. Drug Discov. 22 (2023) 349–350.
[12] J.-e. Zhou, L. Sun, Y. Jia, Z. Wang, T. Luo, J. Tan, et al., Lipid nanoparticles produce chimeric antigen receptor T cells with interleukin-6 knockdown in vivo, J. Control. Release 350 (2022) 298–307.
[13] B. Fadnes, A. Husebekk, G. Svineng, O. Rekdal, M. Yanagishita, S.O. Kolset, et al., The proteoglycan repertoire of lymphoid cells, Glycoconj. J. 29 (2012) 513–523.
[14] S. Mizrahy, I. Hazan-Halevy, N. Dammes, D. Landesman-Milo, D. Peer, Current progress in non-viral RNAi-based delivery strategies to lymphocytes, Mol. Ther. 25 (2017) 1491–1500.
[15] S. Patel, J. Kim, M. Herrera, A. Mukherjee, A.V. Kabanov, G. Sahay, Brief update on endocytosis of nanomedicines, Adv. Drug Deliv. Rev. 144 (2019) 90–111.
[16] S. Sabnis, E.S. Kumarasinghe, T. Salerno, C. Mihai, T. Ketova, J.J. Senn, et al., A novel amino lipid series for mRNA delivery: improved endosomal escape and sustained pharmacology and safety in non-human primates, Mol. Ther. 26 (2018) 1509–1519.
[17] M.P. Lokugamage, C.D. Sago, Z. Gan, B.R. Krupczak, J.E. Dahlman, Constrained nanoparticles deliver siRNA and sgRNA to T cells in vivo without targeting ligands, Adv. Mater. 31 (2019) e1902251.
[18] E. Harris, D. Zimmerman, E. Warga, A. Bamezai, J. Elmer, Nonviral gene delivery to T cells with Lipofecttamine LTX, Biotechnol. Bioeng. 118 (2021) 1693–1706.
[19] M. Schauperl, P.S. Nerenberg, H. Jang, L.-P. Wang, C.I. Bayly, D.L. Mobley, et al., Non-bonded force field model with advanced restrained electrostatic potential charges (RESP2), Communications Chemistry 3 (2020) 1–11.
[20] T. Lu, F. Chen, Multiwfn: a multifunctional wavefunction analyzer, J. Comput. Chem. 33 (2012) 580–592.
[21] M.J. Abraham, T. Murtola, R. Schulz, S. Páll, J.C. Smith, B. Hess, et al., GROMACS: high performance molecular simulations through multi-level parallelism from laptops to supercomputers, SoftwareX 1-2 (2015) 19–25.

[22] J.A. Maier, C. Martinez, K. Kasavajhala, L. Wickstrom, K.E. Hauser, C. Simmerling, ff14SB: improving the accuracy of protein side chain and backbone parameters from ff99SB, J. Chem. Theory Comput. 11 (2015) 3696–3713.
[23] J.F. Nagle, S.T. Nagle, Structure of lipid bilayers, Biochim. Biophys. Acta Biomembr. 1469 (2000) 159–195.
[24] R.T. McGibbon, K.A. Beauchamp, M.P. Harrigan, C. Klein, J.M. Swails, C. X. Hernandez, et al., MDTraj: a modern open library for the analysis of molecular dynamics trajectories, Biophys. J. 109 (2015) 1528–1532.
[25] Z. Lin, M. Bao, Z. Yu, L. Xue, C. Ju, C. Zhang, The development of tertiary amine cationic lipids for safe and efficient siRNA delivery, Biomater. Sci. 7 (2019) 2777–2792.
[26] M. Zhu, G. Nie, H. Meng, T. Xia, A. Nel, Y. Zhao, Acc. Chem. Res. 46 (2013) 622–631.
[27] T. DiTommaso, J.M. Cole, L. Cassereau, J.A. Bugge, J.L.S. Hanson, D.T. Bridgen, et al., Cell engineering with microfluidic squeezing preserves functionality of primary immune cells in vivo, Proc. Natl. Acad. Sci. U. S. A. 115 (2018). E10907-E14.
[28] O. Zupke, E. Distler, A. Jurchott, U. Paiphansiri, M. Dass, S. Thomas, et al., Nanoparticles and antigen-specific T-cell therapeutics: a comprehensive study on uptake and release, Nanomedicine (Lond.) 10 (2015) 1063–1076.
[29] J. Zhang, H. Fan, D.A. Levorse, L.S. Crocker, Ionization behavior of amino lipids for siRNA delivery: determination of ionization constants, SAR, and the impact of lipid pKa on cationic lipid-biomembrane interactions, Langmuir 27 (2011) 1907–1914.
[30] M. Jayaraman, S.M. Ansell, B.L. Mui, Y.K. Tam, J. Chen, X. Du, et al., Maximizing the potency of siRNA lipid nanoparticles for hepatic gene silencing in vivo, Angew. Chem. Int. Ed. Engl. 51 (2012) 8529–8533.
[31] P. Patel, N.M. Ibrahim, K. Cheng, The importance of apparent pKa in the development of nanoparticles encapsulating siRNA and mRNA, Trends Pharmacol. Sci. 42 (2021) 448–460.
[32] S. Liu, Q. Cheng, T. Wei, X. Yu, L.T. Johnson, L. Farbiak, et al., Membrane-destabilizing ionizable phospholipids for organ-selective mRNA delivery and CRISPR-Cas gene editing, Nat. Mater. 20 (2021) 701–710.
[33] J. Bos, L.H. Cisneros, D. Mazel, Real-time tracking of bacterial membrane vesicles reveals enhanced membrane traffic upon antibiotic exposure, Sci. Adv. 7 (2021) eabd1033.
[34] C. Huang, D. Quinn, Y. Sadovsky, S. Suresh, K.J. Hsia, Formation and size distribution of self-assembled vesicles, Proc. Natl. Acad. Sci. U. S. A. 114 (2017) 2910–2915.
[35] F. Daste, C. Sauvanet, A. Bavdek, J. Baye, F. Pierre, R. Le Borgne, et al., The heptad repeat domain 1 of Mitofusin has membrane destabilization function in mitochondrial fusion, EMBO Rep. 19 (2018) e43637.
[36] R.C. Van Lehn, M. Ricci, P.H. Silva, P. Andreozzi, J. Reguera, K. Voitchovsky, et al., Lipid tail protrusions mediate the insertion of nanoparticles into model cell membranes, Nat. Commun. 5 (2014) 4482–4492.
[37] Y.T. Le Guen, C. Pichon, P. Guegan, K. Pluchon, T. Haute, S. Quemener, et al., DNA nuclear targeting sequences for enhanced non-viral gene transfer: an in vitro and in vivo study, Mol Ther Nucleic Acids 24 (2021) 477–486.
[38] C. Cheng, N. Tang, J. Li, S. Cao, T. Zhang, X. Wei, et al., Bacteria-free minicircle DNA system to generate integration-free CAR-T cells, J. Med. Genet. 56 (2019) 10–17.
[39] J.D. Chan, C.M. Scheffler, I. Munoz, K. Sek, J.N. Lee, Y.-K. Huang, et al., FOXO1 enhances CAR T cell stemness, metabolic fitness and efficacy, Nature 629 (2024) 201–210.